Experimental estimates of the energy budget of hydrothermal eruptions; application to 2012 Upper Te Maari eruption, New Zealand

Cristian Montanaro [a,*], Bettina Scheu [a], Shane J. Cronin [b,c], Eric C.P. Breard [c], Gert Lube [c], Donald B. Dingwell [a]

[a] Department of Earth and Environmental Sciences, Ludwig-Maximilians-Universität, Munich Theresienstrasse 41/III, 80333 Munich, Germany
[b] School of Environment, University of Auckland, Private Bag 92019, Auckland 1142, New Zealand
[c] Volcanic Risk Solutions, Institute of Agriculture and Environment, Massey University, Private Bag 11 222, Palmerston North 4442, New Zealand

A B S T R A C T

Sudden hydrothermal eruptions occur in many volcanic settings and may include high-energy explosive phases. Ballistics launched by such events, together with ash plumes and pyroclastic density currents, generate deadly proximal hazards. The violence of hydrothermal eruptions (or explosive power) depends on the energy available within the driving-fluids (gas or liquid), which also influences the explosive mechanisms, volumes, durations, and products of these eruptions. Experimental studies in addition to analytical modeling were used here to elucidate the fragmentation mechanism and aspects of energy balance within hydrothermal eruptions. We present results from a detailed study of recent event that occurred on the 6th of August 2012 at Upper Te Maari within the Tongariro volcanic complex (New Zealand). The eruption was triggered by a landslide from this area, which set off a rapid stepwise decompression of the hydrothermal system. Explosive blasts were directed both westward and eastward of the collapsed area, with a vertical ash plume sourced from an adjacent existing crater. All explosions ejected blocks on ballistic trajectories, hundreds of which impacted New Zealand's most popular hiking trail and a mountain lodge, 1.4 km from the explosion locus. We have employed rocks representative of the eruption source area to perform rapid decompression experiments under controlled laboratory conditions that mimic hydrothermal explosions under controlled laboratory conditions. An experimental apparatus for 34 by 70 mm cylindrical samples was built to reduce the influence of large lithic enclaves (up to 30 mm in diameter) within the rock. The experiments were conducted in a temperature range of 250 °C–300 °C and applied pressure between 4 MPa and 6.5 MPa, which span the range of expected conditions below the Te Maari crater. Within this range we tested rapid decompression of pre-saturated samples from both liquid-dominated conditions and the vapor-dominated field. Further, we tested dry samples at the same pressure and temperature conditions. Results showed that host rock lithology and state of the interstitial fluid was a major influence on the fragmentation and ejection processes, as well as the energy partitioning. Clasts were ejected with velocities of up to 160 m/s as recorded by high-speed camera. In addition to rare large clasts (analogous to ballistics), a large amount of fine and very fine (<63 μm) ash was produced in all experiments. The efficiency of transformation of the total explosive energy into fragmentation energy was estimated between 10 to 15%, depending on the host rock lithology, while less than 0.1% of this was converted into kinetic energy. Our results suggest that liquid-to-vapor (flashing) expansion provides an order of magnitude higher energy release than steam expansion, which best explains the dynamics of the westward (and most energetic) directed blast at Te Maari. Considering the steam flashing as the primary energy source, the experiments suggested that a minimum explosive energy of 7×10^{10} to 2×10^{12} J was involved in the Te Maari blast.
Experimental studies under controlled conditions, compared closely to a field example are thus highly useful in providing new insights into the energy release and hazards associated with eruptions in hydrothermal areas.

* Corresponding author.
E-mail address: cristian.montanaro@min.uni-muenchen.de (C. Montanaro).

1. Introduction

Hydrothermal eruptions are common in broad areas of active and dormant volcanic terrains, where high heat-flow, combined with ground-water close to its boiling temperature, favors rapid generation of steam and fluid-pressure build-up (Browne and Lawless, 2001). These events are particularly hazardous because they often occur with little or no warning (Barberi et al., 1992; Hurst et al., 2014). The 2014 eruption at Mt. Ontake in Japan resulted in 57 deaths (Kato et al., 2015; Yamamoto, 2014), while those that occurred in New Zealand, at Ruapehu in 2007 and Te Maari (Tongariro) in 2012, severely damaged a hikers lodge, which was fortunately unoccupied at the time (Breard et al., 2015; Kilgour et al., 2010). Despite their small volumes, hydrothermal eruptions may be highly energetic and produce extended ash plumes, pyroclastic density currents and widespread ballistic events (Lube et al., 2014). Yet, the processes governing hydrothermal eruptions and associated fragmentation, as well as the energy source propelling them, are poorly understood.

During hydrothermal eruptions, the vaporization of water results in sudden volume increase, producing pressures that are high enough to fragment and eject rocks. Pyroclastic density currents (PDCs) are rarely associated with these eruption types (Browne and Lawless, 2001). Yet, together with ballistic blocks, which are instead commonly ejected, PDCs may represent a major hazard within 1–3 km of the eruptive vent (Breard et al., 2014; Browne and Lawless, 2001; Fitzgerald et al., 2014; Sparks et al., 1997). Field studies of PDC deposits yield information on transport and deposition mechanisms (Breard et al., 2015, 2014; Kilgour et al., 2010; Lube et al., 2014; Montanaro et al., 2016). In contrast, the characterization of fragmentation processes at their source is relatively inaccessible. The mass and spatial distribution of ballistic block dispersal can be used to derive some aspects of eruption dynamics, and their lithologies provide important clues to the depth and mechanisms of explosion (Alatorre-Ibargüengoitia et al., 2012; Breard et al., 2014; Lavallée et al., 2012; Mastin, 1991). In the case of gas expansion-driven blasts, overpressures required to obtain the initial launch velocities typically observed have also been investigated, both theoretically (Fagents and Wilson, 1993) and experimentally (Alatorre-Ibargüengoitia et al., 2011). Field-scale explosion experiments yielded a general relationship between the explosion depth, over-pressure of blasts, and the range of natural volcanic ballistic ejecta observed (Goto et al., 2001; Taddeucci et al., 2013; Valentine et al., 2015; Yokoo et al., 2002).

In hydrothermal eruptions, the fragmentation and ejection of enclosed rock occur largely as the result of the expansion work of a pressurized liquid close to the boiling point (Browne and Lawless, 2001; Mastin, 1995; Thiéry and Mercury, 2009). In such cases the explosive result depends on: 1) the pore-liquid fraction and its physical condition (pressure–temperature) before the eruption (Mastin, 1995); and 2) the lithological and petrophysical properties (e.g. porosity, permeability, strength) of the rock hosting the hydrothermal system (Galland et al., 2014; Haug et al., 2013; Muffler et al., 1971; Thiéry et al., 2010). The first factor (the fluid phase) is effectively the stored explosive energy, while the second factor influences the distribution of energy between the fragmentation process and the kinetic energy imparted to the ballistics (Mastin, 1995; Montanaro et al., 2016; Thiéry and Mercury, 2009).

Here we report on an experimental study designed to investigate the dynamics of hydrothermal explosive eruptions, and primarily the relative influence of the thermodynamic conditions of the fluid phase and the properties of the solid host materials. Experiments were tailored to apply to the August 2012 explosive hydrothermal blast from the Upper Te Maari area on the northern flank of Mt. Tongariro, New Zealand (Fig. 1A). Triggered after a landslide that unroofed part of a hydrothermal system (Procter et al., 2014), this eruption excavated a fissure within altered heterolithic rocks, and produced west- and eastward directed blasts with high-energy ballistics, along with cool (<100°C) PDCs, as well as an ash plume (Breard et al., 2014; Lube et al., 2014; Pardo et al., 2014). Using the westward directed blast as a comparison, we aimed to elucidate: i) the effect of energy source and rock heterogeneity on rock fragmentation, ii) the generation of ballistics and iii) quantify the energy required for rock fragmentation and for the ejecta.

1.1. Initial conditions of the 6th August 2012 Upper Te Maari crater eruption

On the night of 6th August 2012, a partial collapse of the western outer flank of Te Maari crater (Tongariro Volcanic Center, New Zealand; Fig. 1A) triggered the sudden decompression and fragmentation of a sealed, hot hydrothermal system below the crater (Pardo et al., 2014). A ∼20-s-long series of four hydrothermal eruptions occurred, producing a 430-m-long, up to 65-m-wide and 30-m-deep eruptive fissure, immediately south of the Upper Te Maari crater (Fig. 1B).

Breard et al. (2014) showed that the eruption source area is characterized by beds of poorly sorted clay and ashy matrix diamictons, breccias and agglutinates that vary in porosity, grainsize, sorting, thickness, and degree of hydrothermal alteration. Alteration of the rocks in the Te Maari area was driven by a hydrothermal system consisting of a coherent, >100 m thick, condensate layer capping a vapor zone where magmatic steam condensing into circulating meteoric water at equilibrium temperatures of ∼250–300°C (Fig. 1C; Hochstein, 1985). The temperature at the top of this layer is close to boiling. At the nearby Ketetahi, water chemistry indicates a separate, unconnected and hydrothermal system, where the pressure (and temperature) increase linearly with depth, reaching an inferred >5 MPa at the bottom of the condensate layer (Fig. 1C; Walsh et al., 1998; Bromley, 1999). Recent studies based on 3D gravity and magnetic models (Miller and Williams-Jones, 2016) confirm the presence of a very shallow condensate zone below both Ketetahi and the Te Maari area. Injection of magmatic fluids (gaseous and liquid) into the hydrothermal system at least three weeks before the eruption, likely drove up the pressure/temperature state (Fig. 1C; Christenson et al., 2013; Hurst et al., 2014; Jolly et al., 2014). Moreover, minutes before the eruption, an increased seismic activity indicated that microfractures formed in the hydrothermal system; this was probably associated with liquid and gaseous fluids migration through the permeable fracture network, which induced a strong localized pressurization (Fig. 1C; Jolly et al., 2014). This influx of fluids may have destabilized the area that after collapsed (Procter et al., 2014). Finally landsliding and eventual unloading of ∼0.6 MPa was enough to trigger the explosive boiling of the overpressurized hydrothermal fluids (Fig. 1C; Lube et al., 2014; Pardo et al., 2014).

2. Laboratory studies

2.1. Material investigated

The exposed lithology on the western wall of the eruption fissure includes several m-thick breccia and diamicton beds that we observed in the field. These variably hydrothermally-altered deposits, consist of polylithic breccias, interbedded dense and scoriaceous spatter bombs (up to 1 m), along with variably-cemented as well as agglutinated breccias. Most units have a firm/cemented ash fill between clasts, in some cases altered to clay. This is similar to the lithology of the inner Upper Te Maari crater wall (Hobden, 1997; Lube et al., 2014). The same lithologies are recognized
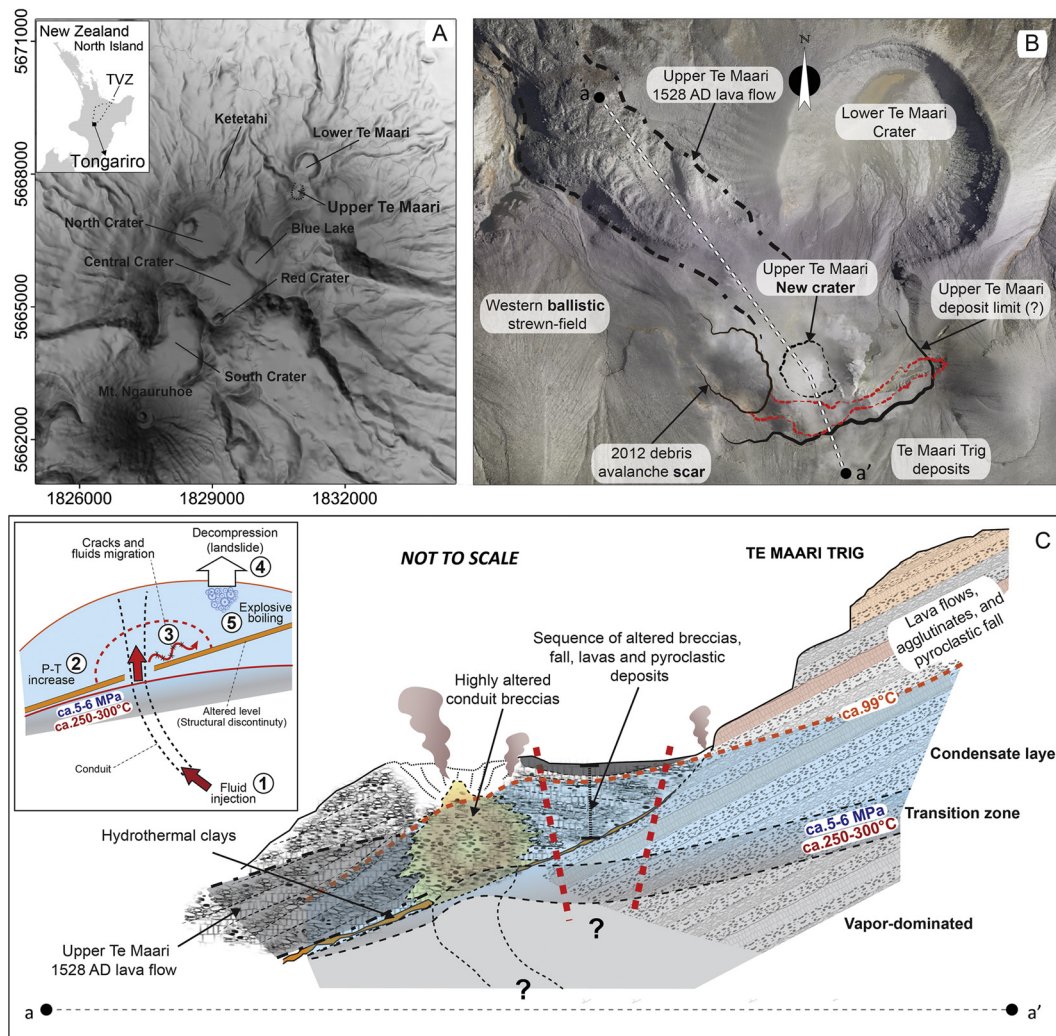
Fig. 1. (A) Shaded relief of the Tongariro Volcanic Centre (in the inlet TVZ: Taupo Volcanic Zone) with locations of the main eruptive centers, including the Upper Te Maari on the northern slope. (B) Post-eruption orthophoto of the Upper Te Maari fissure; new morphological elements as landslide scar (bark brown line) and deposit (dashed pink line) are reported. For a complete map of the western ballistic strewn-field refer to Figs. 6 and 7 of Breard et al. (2014). (C) Conceptual sketch of the Upper Te Maari crater and its hydrothermal system prior to the eruption. The longitudinal profile (aa' in Fig. 1B) shows the inferred condition of the hydrothermal system, as well as the geology, of the Upper Te Maari crater and the northern slopes of Te Maari Trig. Dashed red line indicates the approximate location of the western part of the eruptive fissure. In the inlet a schematic sequence of events occurred before and during the Te Maari eruption: a fluid injection (3 weeks) before the eruption (1); increasing of pressure/temperature state of the hydrothermal system (2); propagation of pressurized fluid along cracks/structural discontinuities minutes prior the event (3); destabilization of the area later affected by flank collapse (4); explosive boiling of the hydrothermal fluids triggered by the decompression following the landslide (5). (D) View of the western fissure from the ballistic field: the eruptive fissure (red line) and delimitation of amphitheater (dark brown line) created by the landslide are reported. Additionally the location of the collected samples from the debris avalanche deposit (D': in the foreground agglutinates attached to dense lava blocks) and an example of agglutinate ballistic clast are shown (D'': block found in the ballistics field). (For interpretation of the references to color in this figure legend, the reader is referred to the web version of this article.)

in ballistic block and large clasts contained in the proximal debris avalanche deposits (Breard et al., 2014; Procter et al., 2014). We collected samples from the proximal debris avalanche deposit (Fig. 1D, D', D''), as representative of the lithology for the source area (breccias and agglutinates). Additionally, the main ballistic block type characteristic of the western ballistic field was sampled. The first sample (TMDA_2B) was a welded agglutinate comprising partially merged, rounded and deformed andesitic lava blocks and lapilli clasts (Figs. 1D', 2). The second sample (TMDA_05) is a breccia of mostly irregular andesitic lava blocks and lapilli incorporated in a firm grey ashy matrix (Fig. 2). The third sample (TMDA_07) is a similar breccia to TMDA_05, but is characterized by lapilli-sized lava clasts showing variable degrees of alteration, contained within a grey to yellowish fine ash matrix (Fig. 2). A ballistic block sample (TMB), which shows similar textures to the breccias, was used for comparison with the density and porosity properties of the debris avalanche samples (Fig. 2). Finally a volcaniclastic sandstone from the northern Eldorado Mountains (NEMSS) of southern Nevada,

USA (Anderson, 1971) was chosen as a control sample (Fig. 2). The sandstone's uniform structure, grainsize, porosity and composition make it a fitting reference material that has the advantage of constant physical properties across all experiment setups. Bulk density, matrix density, and (connected) porosity of dry (oven-dried at 70 °C for 24 h), cored cylinders were measured using a helium pycnometer (Ultrapyc1200e®, Quantachrome) and are reported in Fig. 2 and Table 1.

2.2. Decompression experiments

2.2.1. Methods

We performed experiments in a decompression–fragmentation bomb in the form of a shock-tube apparatus (Fig. 3A; Alatorre-Ibargüengoitia et al. 2010; Mayer et al., 2015; Scheu et al., 2008). In these experiments fragmentation was triggered by decompression of either: (1) argon gas, (2) steam, or (3) water flashing to steam within the connected pore space of the samples. The bomb
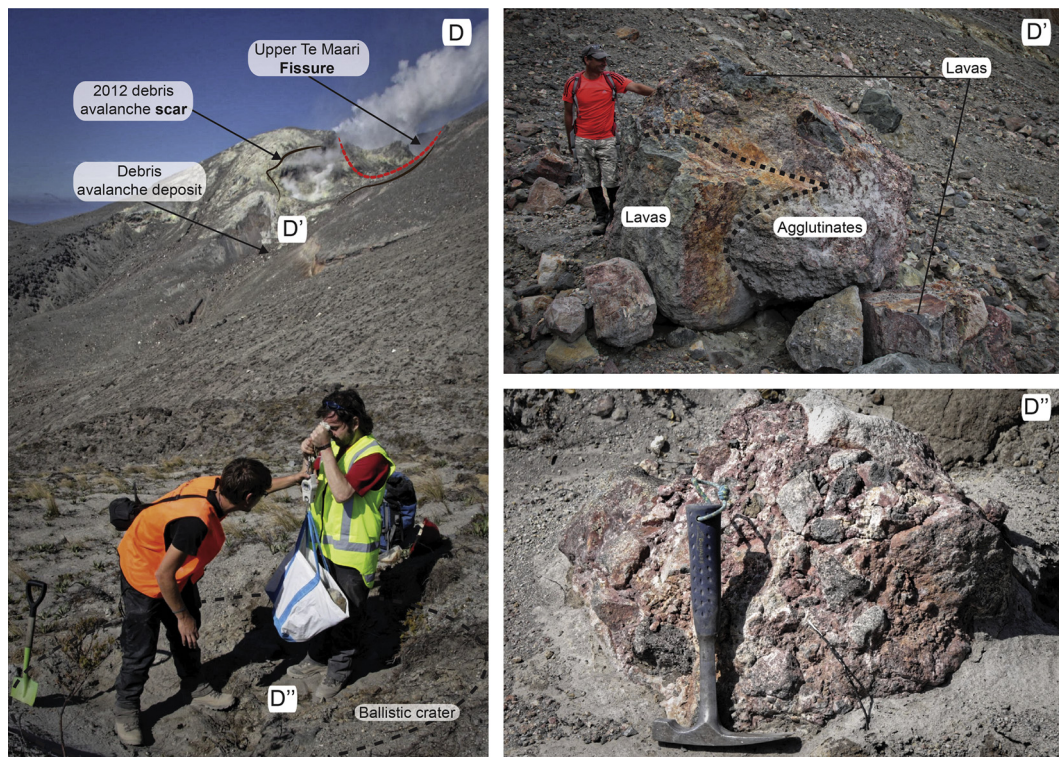
Fig. 1. (*continued*)

	Te Maari Debris Avalanche				Te Maari Bomb	Northern Eldorado Mountain SandStone
	TMDA_2B	**TMDA_05**	**TMDA_07**		**TMB**	**NEMSS**
Porosity	22.8-28.3%	7.4-16.9%	22.2-28.2%		20-25%	23-24%
ρ_{bulk}	1.8-2 g/cm³	2.1-2.3 g/cm³	1.9-2.2 g/cm³		1.8-2 g/cm³	2 g/cm³
ρ_{matrix}	2.5-2.6 g/cm³	2.5 g/cm³	2.7-2.8 g/cm³		2.4-2.5 g/cm³	2.6 g/cm³

Fig. 2. Photographs of the three investigated sample series from Te Maari debris avalanches blocks (left). Samples show differences in macroscopic texture, color and particle size in respect to a collected ballistic block, and the homogeneous sandstone used as control sample (right). Below each sample porosity, bulk and matrix density are reported.

allows for the accurate control of temperature, gas overpressure and decompression rate in order to best represent variable volcanic and hydrothermal conditions. The shock-tube apparatus is capped by a stainless steel tank ($l = 3.0$ m; $d = 0.4$ m) at ambient pressure and temperature, which is used to collect the experimentally-generated fragmented material. The sample is loaded into a high pressure–temperature steel autoclave (Fig. 3A). To reduce the influence of large lithic enclaves (up to 30 mm in diameter) within the samples, a special set-up was built to allow samples of up to 34 mm diameter and 70 mm length (Montanaro et al., 2016). A series of thin metal (copper or aluminium) diaphragms separate the upper low-pressure chamber from the autoclave. Controlled rupture of the diaphragms leads to a rapid decompression of the high-pressure autoclave producing a rarefaction front, which propagates downwards into the autoclave and through the sample. Samples are fragmented by sudden expansion of (1) argon gas or (2) steam, in a brittle, layer-by-layer fashion (Alidibirov and Dingwell, 2000). For the case (3) of vaporization of water, fracturing

is less dependent on the decompression front, being more sensitive to the orientation of pore space and, possibly, pre-existing fractures (Rager et al., 2014). A transparent section at the bottom of the large chamber allows monitoring of the sample ejection with a high-speed camera (Fig. 3). The fragmented material is collected from the large chamber and its grain-size distribution was analyzed using dry sieving at half-phi steps (between -4.5 and 4.5 phi).

In order to span the range of expected conditions below the Te Maari crater (Sec. 1.1), temperatures ranging from 250 °C and 300 °C, and pressure between 5 MPa and 6 MPa were chosen for the experiments (Fig. 1; Walsh et al., 1998), in contrast to the triggering pressure change of 0.6 MPa. A series of control experiments (1), where fragmentation is driven by argon expansion (AE), were performed on dry samples at similar temperatures and pressures (300 °C and 5 MPa) as for condition (2). For the latter type pre-saturated samples were heated in a vapor-dominated field causing steam expansion (SE). For condition (3)

Table 1
Properties of the investigated material.

Sample	Mass (g)	$V_{calc.}$ (cm³)	$\rho_{calc.}$ (g/cm³)	$V_{meas.}$ (cm³)	$\rho_{meas.}$ (g/cm³)	Porosity (%)
Argon Expansion (AE)						
TMDA_2b_05	115.7	62.8	1.8	45	2.6	28.3
TMDA_07_13	126.3	63.1	2	46.6	2.7	26.1
NEMSS 10_08	127.7	63.8	2	49.1	2.6	23
Steam Expansion (SE)						
TMDA_2b_08[#]	122.8	61.8	2	47.7	2.6	22.8
TMDA_2b_10[#]	118.9	60	2	45.8	2.6	23.7
TMDA_05_01[#]	130.9	63	2.1	52.4	2.5	16.9
TMDA_05_07[#]	145.9	64.7	2.3	59.4	2.5	8.2
TMDA_07_11	122.9	63.2	1.9	45.4	2.7	28.2
TMDA_07_14	124.2	62.9	2	45.5	2.7	27.7
NEMSS 10_04	128.7	64.5	2	49.4	2.6	23.4
NEMSS 10_09	124.7	62.7	2	47.9	2.6	23.6
Steam Flashing (SF)						
TMDA_2b_01	104.5	54.7	1.9	41.2	2.5	23.2
TMDA_2b_09	118.8	61	1.9	46	2.6	24.5
TMDA_05_06[#]	149.1	64.7	2.3	59.7	2.5	7.6
TMDA_05_08[#]	146.6	64.7	2.3	59.9	2.5	7.4
TMDA_07_03	139.4	64.6	2.2	50.2	2.8	22.2
TMDA_07_08	104.7	51.8	2	37.8	2.8	26.1
NEMSS 10_01	126.9	64.1	2	48.7	2.6	24.1
NEMSS 10_07	125.3	62.8	2	48.1	2.6	23.5

additional argon gas input, allowed maintaining a liquid-dominated field causing steam flashing (SF) (Fig. 3B; Mayer et al., 2015; Rager et al., 2014).

Each rock sample was mounted into a cylindrical steel crucible. For type (1) experiments, the sample was directly placed into the autoclave. For type (2) experiments, ~15 g of distilled water was added (as calculated via steam tables) to achieve the desired pressurization within the known connected pore space of the sample, and in the remaining autoclave chamber space, via steam pressure. Temperature was raised to the boiling point, and the gases generated upon vaporization increased the pressure in the autoclave until the targeted dwell conditions of 5 MPa and 300 °C were reached (Fig. 3B). Heating and dwelling lasted ~90 min, followed by 10 min of equilibration before triggering. For type (3) exper-

iments, mounted samples were submerged in water and placed under a vacuum for at least 72 h to maximize water saturation throughout the porosity. In this case, the heating and dwelling process lasted ~60 min, with an additional 10 min for equilibration. During the sudden decompression of the system, the liquid–vapor phase boundary of water is crossed (Fig. 3B).

2.3. Results

2.3.1. Grain-size distribution

The results of the grain-size analysis are discussed with respect to their lithology (breccia, agglutinate, and sandstone control sample) and the experimental conditions (AE: argon expansion, SE: steam expansion, and SF: steam flashing). Similar grain-size dis-
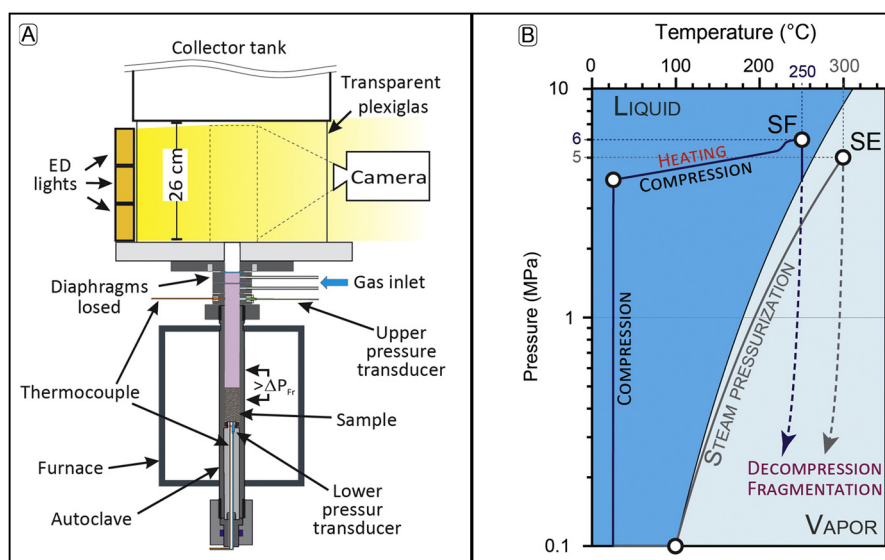

Fig. 3. (A) Sketch of the fragmentation apparatus. (B) Water phase diagram showing the experimental path followed during each experiment. In the case of steam-flashing (SF) condition, samples were pressurized up to approximately 4 MPa, then heated at 15 °C/min. A final pressure of 6 MPa was obtained at the end. The overall pressurization, heating and dwelling process lasted for about 50–60 min. For the steam expansion (SE) case, ~15 g of distilled water was added to achieve the desired pressurization via steam pressure. After boiling started, vapor increased the pressure in the autoclave until the targeted dwell conditions of 5 MPa and 300 °C were reached. Heating and dwelling process lasted ~90 min, and after 10 min of equilibration the experiment was triggered. A set of diaphragms allows reproducible pressurization of the sample using Argon gas or steam. Modified after (Scheu et al., 2006; Mayer et al., 2015).
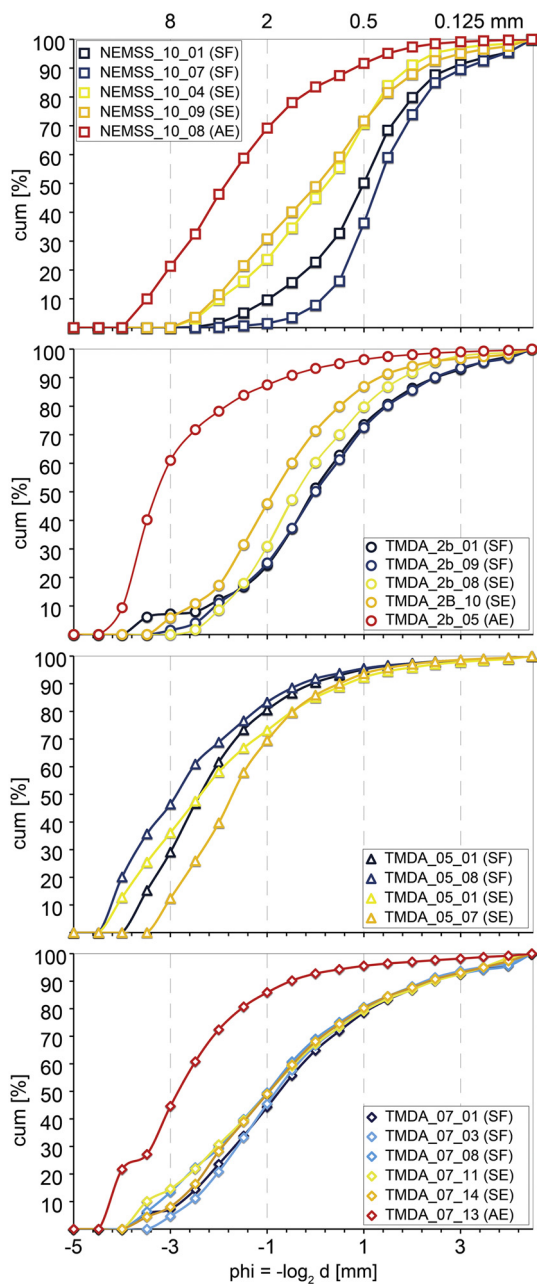
Fig. 4. Cumulative grain size distribution plots showing the weight fractions of particles after rapid decompression experiments at different experimental conditions in half-phi steps (phi = − log₂ d, with d = particle diameter in mm). For each sample series result represent the size distribution produced by steam-flashing (SF), steam expansion (SE) and argon expansion (AE). The particle size is decreasing to the right in all plots.

tributions are produced from experiments under each condition for the different lithologies, confirming experimental reproducibility despite the heterogeneous material (Fig. 4; Table 2).

1) NEMSS: the control sample generally produces fewer coarse clasts than the Te Maari samples. The coarsest grain-size distribution (Md −1.67 phi), results from AE, with SE (−0.08 to −0.01 phi) and SF (0.93 to 1.41 phi) showing progressively finer grainsize. Fines (>4 phi) production increased from 0.3% for the AE experiments, to 1.5–2.4% for SE and 4.5% for SF.

2) TMDA_2B samples contain common lava clast enclaves within porous agglutinate. A very coarsely-skewed grain-size distribution, with a median diameter of −2.9 phi, resulted from the AE experiment, but finer overall clast size were produced under

SE (−0.23 to −0.72 phi) and SF samples (0.06 to 0.09 phi). In the case of fines (>4 phi), AE produced 0.4 wt%, while SE generated 1.2–1.9 wt% and SF 2.6–3.1 wt%. Notably, under the SE condition only around two thirds of the sample fragmented, while the higher porosity of the used sample (28.3%) allowed for a total AE fragmentation.

3) TMDA_05 has the largest lava enclaves (up to 6 cm long) embedded in a fine ash matrix, and show the lowest porosity values (down to 7.4%). These samples generally produced the coarsest grain-size distributions amongst the Te Maari samples. Moreover samples only partially fragment (from 2/3 to 1/3 of the whole sample) under both SE and SF conditions, and did not fragment under AE. The mean diameter for the SE case (−2.11 to −1.57 phi) is slightly lower than that for the steam flashing samples (−2.64 to −2.18 phi). Both conditions produced few fines (>4 phi), with 0.6–1 wt% resulting from the SE and 0.7–1 wt% generated by SF.

4) TMDA_07 samples contain few lava enclaves, but the fine matrix has high porosity (up to 28%). A very coarse grain-size distribution (Md −2.71 phi) is produced by AE, with similar finer clast sizes produced by SE (−0.68 to −0.76 phi) and SF experiments (0.53 to 0.80 phi). The amount of fines produced (>4 phi) increased from 0.8% for AE case, to 1.7–2.8 wt% for SE, and 3.7–4.5 wt% for SF.

2.3.2. Ejection velocities

Particle ejection velocities for repeated experiments (to account for sample heterogeneities) were computed from the displacements of individual particles tracked across five successive frames of the high-speed footage. An average speed of those particles at the absolute flow front was calculated using (≥5) particle velocities (Mayer et al., 2015). In all experiments we observed that ash particles <2 mm are initially ejected while being well-coupled with the gas phase. These gas-coupled fine particles traveled two to three times faster than the gas-decoupled >2 mm (lapilli) particles (Table 1). The lapilli particles thus displayed a ballistic-like behavior. For a few steam flashing (SF) experiments the initial part of the plume was obscured by large vapor clouds and only the ejection velocities of >2 mm particles could be measured (Table 2).

The ejection velocity of the >2 mm particles in the ejection front varied according to both porosity and experimental conditions (Fig. 5A, B). Generally the SF experiments produced the fastest ejecta (32 ± 2 to 136 ± 7 m/s), with SE intermediate (21 ± 1 to 85 ± 9 m/s) and AE slowest (40 ± 2 to 53 ± 5 m/s). Under the SF conditions, fragments produced by the TMDA_07 series were the fastest observed in all experiments, while TMDA_05 ejecta were the slowest (46 ± 3 m/s). The same pattern was observed in the SE case, with TMDA_07 particles as the fastest (71 ± 5 m/s), TMDA_2B intermediate (35 ± 3 m/s), and TMDA_05 showing one slow example (25 ± 1 m/s), and one fast (85 ± 5 m/s). The latter was affected by a large cavity later seen in the partially fractured sample and was treated as anomalous. For the AE experiments the ejection velocities were uniform for all lithologies.

3. Energetic considerations

3.1. Theoretical background

The explosive energy during the experiments was sourced from: i) energy released by argon expansion, ii) steam expansion, and iii) instantaneous and adiabatic vaporization (steam flashing). Similarly, the explosive energy within hydrothermal systems is controlled by the pressure and temperature conditions, which, in turn, control the fluid phase prior to explosive failure.

The explosive energy released by the expansion work of the fluids (gas or liquid) in the rock pore space, from the breaking

Table 2
Experimental conditions and results.

Sample	H_2O/Ar[a]/St[a] (g)	Porosity (%)	T (°C)	P (MPa)	E_{expl-R} (J)	E_{expl-I} (J)	E_{Vol} (MJ/m³)	E_{Mass} (kJ/kg)	v_{Eject} (±Err) (m/s) <2 mm	v_{Eject} (±Err) (m/s) >2 mm	wt% >4 phi	Md phi
Argon Expansion (AE)												
TMDA_2b_05	0.9	28.3	300	5	122		1.7	0.9	56 (±2)	53 (±5)	0.4	−2.9
TMDA_07_13	0.8	26.1	300	5	134		1.6	0.9	55 (±3)	52 (±3)	0.8	−2.7
NEMSS 10_08	0.7	23	300	5	121		1.4	0.7	70 (±19)	40 (±2)	0.3	−1.7
Steam Expansion (SE)												
TMDA_2b_08[b]	0.3	22.8	305	5	86		1.4	0.7	92 (±12)	35 (±3)	1.2	−0.2
TMDA_2b_10[b]	0.3	23.7	298	5	85		1.4	0.7	89 (±6)	21 (±1)	1.9	−0.7
TMDA_05_01[b]	0.2	16.9	303	5	64		1	0.5	121 (±4)	85 (±5)	1	−2.1
TMDA_05_07[b]	0.1	8.2	310	5	35		0.5	0.2	79 (±9)	25 (±1)	0.6	−1.6
TMDA_07_11	0.4	28.2	298	5	113		1.8	0.9	96 (±7)	71 (±5)	1.7	−0.8
TMDA_07_14	0.4	27.7	285	5	104		1.7	0.8	81 (±7)	69 (±3)	2.7	−0.7
NEMSS 10_04	0.5	23.4	296	5	92		1.4	0.7	127 (±13)	85 (±9)	1.5	0.1
NEMSS 10_09	0.4	23.6	300	5	88		1.4	0.7	134 (±20)	79 (±6)	2.4	0
Steam Flashing (SF)												
TMDA_2b_01	11.7	23.2	252	6		618	11.3	5.9	156 (±11)	120 (±4)	2.6	0.1
TMDA_2b_09	13.2	24.5	250	6		697	11.4	5.9	157 (±12)	125 (±5)	3.1	0.1
TMDA_05_06[b]	6	7.6	262	6		340	5.3	2.3	/	32 (±2)	0.7	−2.2
TMDA_05_08[b]	6.1	7.4	252	6		323	5	2.2	77 (±14)	46 (±3)	1	−2.6
TMDA_07_03	13.8	22.2	256	6		781	12.1	5.6	/	136 (±7)	3.7	−0.5
TMDA_07_08	12.1	26.1	254	6		639	12.3	6.1	/	134 (±7)	4.5	−0.8
NEMSS 10_01	14.7	24.1	260	6		830	12.9	6.5	177 (±13)	/	4.5	0.9
NEMSS 10_07	14.9	23.5	250	6		787	12.5	6.3	200 (±22)	118 (±11)	4.5	1.4

[a] The argon (Ar) and steam (St) mass have been calculated considering their density at the experimental temperature and pressure.
[b] Only partial fragmentation of the sample occurred (from 1/3 for the TMDA_05 to 2/3 for the TMBA_2B).

pressure of the pore and up to the atmospheric pressure, is given by:

$$E_{Expl} = m \times \Delta U \quad (1)$$

where E_{Expl} is the available explosive energy which can be released in the expansion of the fluids (J), m is the mass of fluid in the pores at the moment of the failure (g), ΔU is the difference in internal energy of the fluid under the conditions before and immediately after the expansion (J/g). The maximum amount of work that can be extracted from an expansion, and thus the associated explosive energy, depends upon the thermodynamic path (Mastin, 1995; Thiéry and Mercury, 2009).

For the AE and SE we assume that both argon and steam behave as ideal gases and that the expansion is adiabatic and reversible (isentropic). Thus the expansion work must be equal to the variation in internal energy of the fluid ΔU:

$$\Delta U = -P_{atm} \times \Delta V \quad (2)$$

integrating and introducing the relationship $P \times V^\gamma = $ constant (γ being the ratio of specific heats), the energy of expanding gas (argon or steam) can be calculated (Prugh, 1991) as:

$$E_{Expl-R} = \left[\frac{P \times V}{\gamma - 1} \right] \times \left[1 - \left(\frac{P_{atm}}{P} \right)^{\left(\frac{\gamma-1}{\gamma} \right)} \right] \quad (3)$$

where E_{Expl-R} is the reversible explosive energy released (J), P_{atm} is the atmospheric pressure (1 bar), V is the initial volume of argon or steam (m³), and P is the pressure (bar) in the rock pore space just before the explosive failure. The different densities, and therefore masses of argon and steam at different pressure–temperature conditions were also accounted for (Table 2).

For the energy calculations of SF experiments, an irreversible approach (Planas-Cuchi et al., 2004) was preferred over a reversible one (Mastin, 1995). This is because the latter approach assumes that the fluid expands isentropically as an ideal gas, and ignores any energy consumption through internal friction. Planas-Cuchi et al. (2004) modified this approach by equating the internal energy change of a fluid (water) to the irreversible work performed

as the expanding vapor pushes against the surrounding medium. They also assumed that immediately after the expansion, there is liquid–vapor equilibrium at atmospheric pressure and at the corresponding saturation temperature. This assumption is much closer to the real situation and allows less conservative estimations of overpressure by taking irreversibility factors into account such as: friction, heat loss, unrestrained expansion of a gas, and others. The analytical solution of equation (2) applied to a mass of liquid which vaporizes, enables calculation of the flashed steam fraction accounting for irreversibility (Planas-Cuchi et al., 2004; Thiéry and Mercury, 2009) as:

$$x = 1 - f = 1 - \left(\frac{[P_{atm} \times (v_{initial} - v_{vap})] - U_{vap} + U_{initial}}{U_{liquid} - U_{vap} + [P_{atm} \times (v_{liq} - v_{vap})]} \right) \quad (4)$$

where x and f represent the steam and liquid fraction respectively, v is the molar volume, and U the internal energy. $U_{initial}$ (J/mol) and v_{inital} (m³/mol) are calculated at the initial condition of the system. U_{liq} (J/mol), v_{liq} (m³/mol), U_{vap} (J/mol) and v_{vap} (m³/mol) are all calculated at 100 °C and 1 bar (atmospheric-pressure boiling-point). Thiéry and Mercury (2009) demonstrated that an isenthalpic hypothesis yields a good approximation of the irreversible case. Under this assumption the irreversible energy of an expanding saturated liquid can be calculated as:

$$E_{Expl-I} = m_w \times \left(P_{atm} \times [(1 - f) \times v_{vap} + f \times v_{liq} - v_{initial}] \right) \quad (5)$$

where E_{Expl-I} is the irreversible explosive energy released (in J), and m_w is the mass of water (g) in the pore space.

3.2. Explosive energy during decompression experiments

The estimated explosive energy due to the work of the expanding fluids (argon and steam) was investigated in relation to the experimental conditions. The argon (AE) and steam expansion (SE) experiments were run at ∼300 °C and 5 MPa, whereas the steam
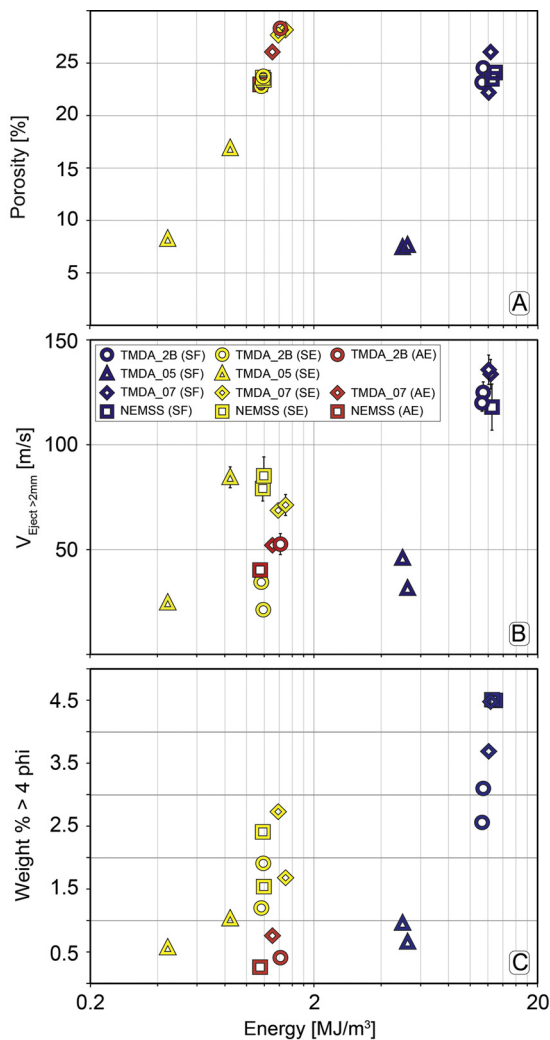
Fig. 5. Experimental results of (A) sample porosity, (B) particles ejection velocity, and (C) produced weight % fines (>4 phi) as a function of the explosive energy per unit volume in the presence of steam-flashing (SF), steam expansion (SE) and argon expansion (AE). Results are also reported in Table 2.

flashing (SF) experiments were carried out at ~250°C and 6 MPa. The explosive energy varied in agreement with both porosity and explosive source (Fig. 5A; Table 1). Furthermore, there was a direct positive relationship between explosive energy and proportion of fine material produced (Sec. 2.3.1), as well as with ejection velocities observed (Sec. 2.3.2) (Fig. 5B, C; Table 2).

For argon and steam expansion experiments, equation (3) was used to estimate the reversible energy E_{Expl-R}, while equations (5) served to estimate the irreversible energy E_{Expl-I} for the steam flashing conditions. In general, the steam-flashing produced the most energetic explosions (322.6 to 830 J), whereas expansion of both steam (35 to 113 J) and argon (87 to 109 J) resulted in less powerful events. Results in terms of energy per unit volume (E_{Vol}) of fluid prior to explosive failure are used to discuss the energies of the different samples (Table 2). Energetic values per unit volume (E_{Mass}) are also reported in Table 2.

1) The control sandstone NEMSS used for the AE and SE condition experiments have an open porosity range of 23–24.1%, and produced an energy release of 1.4 MJ/m³ for both conditions. For the SF case, samples retained 14.7–14.9 g of water and released 12.5–12.9 MJ/m³.

2) For TMDA_2B, an open porosity of 22.8–28.3% resulted in an energy release of 1.7 MJ/m³ for AE and 1.4 MJ/m³ for SE. Under

SF condition, and with 11.7–13.2 g of retained water, an energy release per unit volume of 11.3–11.4 MJ/m³ is calculated.

3) The dense TMDA_05 did not fragment under AE conditions. For the SE condition the low porosity (8.2 and 16.9%) produced a volumetric energy release of 0.5 and 1 MJ/m³. Only 6 g of water were retained under SF, resulting in a volumetric energy release of 5 to 5.25 MJ/m³. In both cases the energy was not sufficient to fully fragment the sample.

4) The highly porous TMDA_07 samples (26.1 to 28.2%) under AE and SE conditions produced energy release of 1.7 to 1.8 MJ/m³. For SF conditions samples retained 12.1 and 13.8 g of water, which released 12.1–12.3 MJ/m³.

4. Discussion

4.1. Pressure–temperature effect: steam flashing (SF) versus steam expansion (SE)

The main finding of our experimental results is that eruptions of the Te Maari rock (and a homogeneous sandstone with comparable total porosity) are far more energetic when driven by the flashing of high-temperature and high-pressure liquid water into a vapor phase, versus simple steam or dry-gas expansion. Therefore the energy is strongly influenced by the pre-existing pressure–temperature conditions of an unroofed hydrothermal system. Pressure and temperature also controls the fluid state, and thus whether flashing, or simple steam expansion, occurs, or a combination of both (Mastin, 1995; Thiéry and Mercury, 2009). A temperature range between 250 and 300°C, with a confining pressure varying from 5 to 6 MPa, was used in this study (Sec. 1.1). Within this range both liquid and vapor water could be filling pores. These conditions agree well with those estimated below the Te Maari hydrothermal system prior to the eruption, when the pressure/temperature state was pushed up by the rise of magmatic fluids (Fig. 1C; Hurst et al., 2014; Jolly et al., 2014).

4.2. Porosity and rock texture effects

Heterogeneous tuff breccia with lithic particles 2–3 m in diameter and agglutinates, showing a large range in porosity (7.6–28.3%), were recognized in large blocks of the debris avalanche deposits, and in outcrops in the walls of the western eruptive fissure (Breard et al., 2014). Porosity of rocks is a key factor in controlling the explosive behavior of a volcanic system (Mueller et al., 2011; Scheu et al., 2006; Spieler et al., 2004), particularly in terms of energy storage, which drives the fragmentation process (Kueppers et al., 2006). Under all our experimental conditions (AE, SE and SF), explosive energy increases with porosity (Fig. 7A; Table 2). The fragmentation process we observed was not only strongly influenced by porosity, but also by the heterogeneity of the rock and the presence of dense and strong lithic enclaves and agglutinate. Compared with the homogeneous control sandstone (NEMSS), the breccias and agglutinates produced distinct polymodal grain-size distributions under all the investigated conditions. The lowest porosity tuff-breccia (~7%), rich in large and dense enclaves embedded in a firm ash matrix, only partially fragmented under SF and SE conditions, and not at all under AE. The agglutinates with high porosity (28%), but with a slightly more compacted agglomerate matrix, generated less fine material. By contrast, tuff breccia with higher porosity (up to 28%), and smaller enclaves in a weaker fine ash matrix, produced the most fine fragments and poorly sorted ejecta in all cases (Fig. 5C, 6). Across all the experiments, the presence of dense enclaves accounted for the production of coarser clasts (Fig. 6).
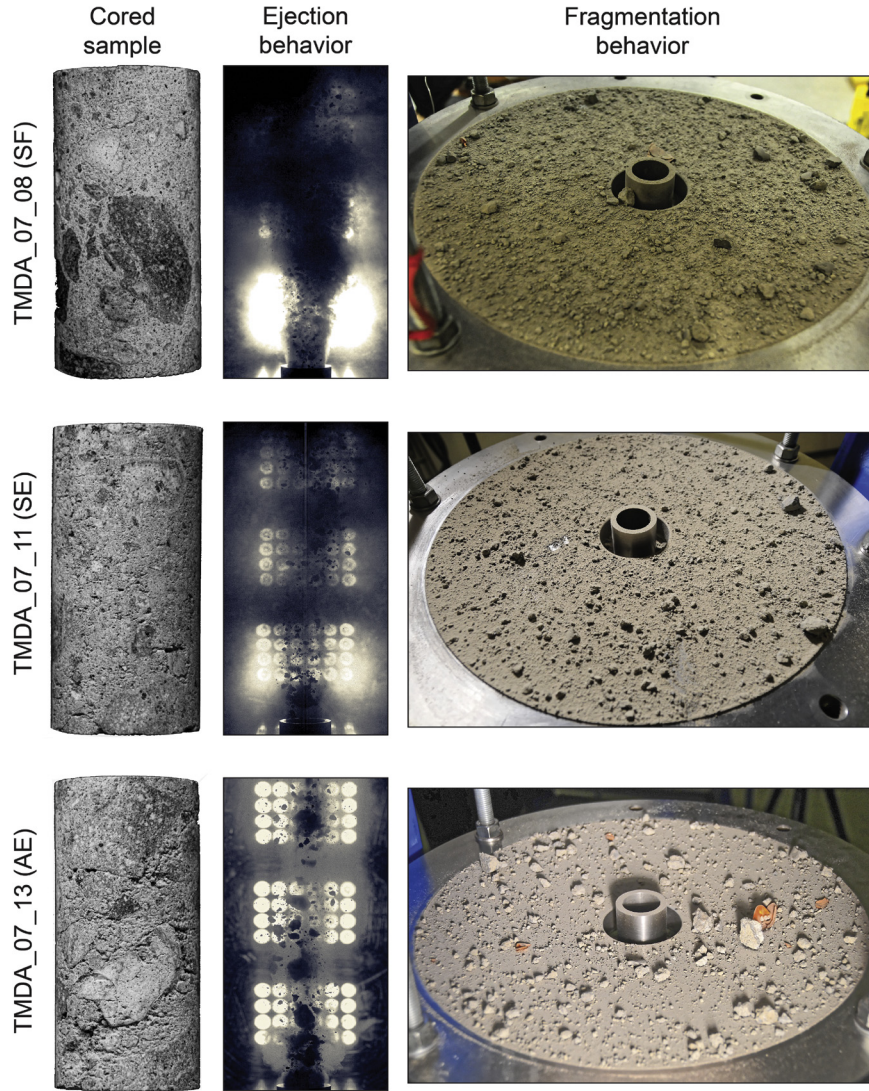
Fig. 6. From cored to fragmented sample: differences in ejection and fragmentation processes produced under steam-flashing (SF), steam expansion (SE) and argon expansion (AE) conditions. Example from TMDA_07 series sample. From SF to AE there is a clear increase in the size of ejected clasts, with a less well-defined plume of fine material formation (frame are taken at the same ejection time). The different rate of coarse and fine material production is also evident in the collector tank base.

4.3. Ejection velocity of fragmented heterogeneous breccias

The ejection velocity of the gas–particle mixture from our experiments increased with the explosive energy (Fig. 5B). Steam flashing (SF) also increases gas volume that further powers the ejection processes (Mastin, 1995; Mayer et al., 2015). This was shown by the high particle ejection velocities under the SF conditions (up to ~160 m/s), across all sample series (Fig. 5B; Table 2). The ejection speed of particles in the presence of SF were likely underestimated, because the initial gas expansion obscured early identification of particles in the images. Velocities reached for the SE and AE cases were only a half to a third of those produced in the steam flashing case. Additionally, results of the SF experiments show that the very fine material was also ejected at higher velocities (50 to ~160 m/s) than the lapilli-sized clasts (>2 mm). Interestingly, TMDA_2B and 07 series samples were the only ones to eject particles >2 mm at high velocities (120 to 136 m/s) under SF conditions.

4.4. Energy partitioning

The factor E_{Expl} (Sec. 4) estimates the amount of energy that can be converted into fragmentation (ΔE_f), gravitational potential

(ΔE_p), kinetic (ΔE_k) and all other forms of mechanical energies (noted as ΔE_d) such as elastic deformation, shock waves, etc. Thus, the energetics of fluid flows and eruption phenomena can be assessed by using a modified form of Bernoulli's equation (Mastin, 1995; Thiéry and Mercury, 2009):

$$E_{\text{Expl}} = \Delta E_f + \Delta E_p + \Delta E_k + \Delta E_d + \text{``frictional-terms''} \qquad (6)$$

The last term accounts for the energy consumption due to rock–fluid internal friction. Expanding gas trapped in pores is the largest energy source, which is partially consumed by fragmentation, and partially converted into kinetic energy to expel the fragments (Alatorre-Ibargüengoitia et al., 2010; Alidibirov and Dingwell, 2000). A minimum pressure differential, the fragmentation threshold (P_{fr}), must be overcome to fully fragment a pressurized porous rock. This threshold is inversely related to the porosity (Spieler et al., 2004). Koyaguchi et al. (2008) proposed a fragmentation threshold criterion based on the Griffith theory for crack propagation through elastic media with a homogeneously distributed porosity. The model of crack propagation from the inner to the outer pore wall, considers the tensile strength of the solid phase and the tangential stress at the outer pore wall, and is defined as:

$$P_{fr} = \frac{2 \times \sigma_3 \times (1 - \Phi)}{3 \times \Phi \times \sqrt{\Phi^{-1/3} - 1}} \tag{7}$$

where Φ is the porosity and σ_3 is the effective tensile strength ($\sigma_3 = 2.18$; Koyaguchi et al., 2008). The estimated values in this study can be considered as a minimum fragmentation threshold for a homogeneous rock, such as the case of the control sandstone (NEMSS). Yet, deviation from this value should be expected when samples are heterogeneous (Scheu et al., 2006). The Te Maari host material is highly heterogeneous in porosity, strength, and matrix properties, which may result in an increase of the fragmentation threshold.

The variable porosity of the breccias and agglutinates ($\sim$7 to $\sim$28%) used in our study indicates that fragmentation requires gas overpressure P_{fr} from at least 5 to 15.4 MPa. Using the porous volume of the experimental samples, and the calculated threshold P_{fr} in equation (3), a minimum fragmentation energy ΔE_f ranging from 89.1 to 110.6 J was estimated. This fragmentation energy accounts for the primary sequence of fracturing (Fowler et al., 2010; McGuinness et al., 2012), whereas secondary fragmentation consumes less energy, which is likely negligible here. The estimated energy threshold is exceeded by an order of magnitude for the SF energy source case. Instead the threshold values were similar to the explosive energy estimated for the SE and AE cases. This is consistent with the incomplete or failed fragmentation for the least porous samples of the TMDA_05 and 2B series.

The minimum kinetic energy ΔE_k associated with the ejected fine material and the lapilli-sized clasts was also assessed. For the calculations the ejection velocities (v) produced under the SF conditions were used, since these are most likely to represent the process generating the ballistic field of Te Maari (Breard et al., 2014; Fitzgerald et al., 2014). We choose two size thresholds for the calculations: the 1 mm as upper limit of the faster particles, and 2 mm as lower limit for the slower particles. Particles were assumed to have spherical shapes and a density equal to those measured one for the sample ($\rho_{measu.}$; Table 2). By neglecting the energy dissipated in the accompanying seismic wave, we calculated mass (m) and kinetic energy of the ejected projectiles using:

$$\Delta E_k = 1/2 \times m \times v^2 \tag{8}$$

Thus we estimated a kinetic energy range between 0.03 to 0.13 J for particles of 1 mm size, and between 0.1 to 0.9 J for the 2 mm size.

Finally for the energetics estimate under SF conditions we evaluated the energy conversion ratio of the fragmentation and kinetic energy over the (maximum) explosive energy. This ratio defines how efficiently the available energy budget is converted in other forms. The ratio of fragmentation to explosive energy ranges from 9.5 to 15.2%, whereas the conversion ratio to kinetic energy is on the order of 0.02% for the 1 mm size, and up to 0.1% for the 2 mm particles. These estimates of kinetic energy concern specific grainsizes; however in nature the gas–solid coupling and momentum transfer will differ from these non-scaled experiments.

4.5. Eruption dynamics and energetics of the westward directed plume

The 6th August 2012 hydrothermal eruption at Upper Te Maari was set off by a landslide (Jolly et al., 2014) that unloaded approximately 0.6 MPa of lithological load (Procter et al., 2014). This sudden pressure drop appeared to destabilize the hydrothermal system, leading to its sudden decompression. Magmatic gases injected into the system prior to the eruption (Christenson et al., 2013; Hurst et al., 2014), along with considerable seismic activity indicating both brittle and fluid motions (Jolly et al., 2014), produced a high pressure contrast between the deep hydrothermal system and the surface. Thus decompression triggered an intense boiling and flashing of superheated liquid water into steam, propelling the eruption (Sec. 1.1; Fig. 1C). The geological discontinuities within the hydrothermal system (Fig. 1C) and the landslide failure geometry caused lateral jetting (Lube et al., 2014). The most energetic westward-directed blasts produced widespread pyroclastic surges, and the highest density ballistic strewn-field (Breard et al., 2014). These west-directed ballistics are the only ones that include blocks with a distinctive tuff breccia and agglutinate lithology (TMBA_2B and 7), matching the location of shallow inclined beds of cemented tuff breccia and agglutinate (Fig. 7). An exposed ridge separated blast fissures to the east and west. This was composed of hard, low porosity lavas and possibly also strongly cemented rock similar to the TMDA_05 breccia (Fig. 7).

Based on the experimental results it is clear that the steam-flashing of hydrothermal fluids (mainly water) propelled the Upper Te Maari eruption. Estimations of fragmentation threshold (Sec. 4.4) and experimental results also suggest that, despite their different degree of alteration, the rocks in the source area (breccias and agglutinates) had a certain degree of cohesive strength. This would have helped to support pressure accumulation before the failure of the hydrothermal system. After the initial pressure drop, the flashing of pressurized liquid water into a vapor phase generated an explosive boiling-front that penetrated downwards into the hydrothermal reservoir (Fig. 7; McKibbin et al., 2009). The volume lost from the fissure area is likely greater than the volume of the main fissure scar (Procter et al., 2014; Lube et al., 2014), and post-event fill materials belie a greater subsurface volume, and a deep excavation. Considering this we estimate a minimum explosive energy for the western blast of 7×10^{10} to 2×10^{12} J. Our estimation is based on the following assumptions: 1) an excavation depth between (observed) 20 and (inferred) 50 m over $\sim$11,000 m^2 (Procter et al., 2014), which equates to a volume range between 200,000 and 550,000 m^3; 2) a source rock composed by tuff breccias and agglutinates with a porosity range between 7.5 and 28% (Table 2); 3) an experimentally-estimated energy release per unit volume of 5 to 12.9 MJ/m^3; and 4) a wide almost homogeneous overpressurization of the southern part of the hydrothermal system prior the eruption. The last assumption implies that during most of the eruption, steam formation was approximately constant. Further, if the reservoir conditions (overpressurization, temperature, etc.) were constant, the steam flashing and fragmentation processes were too rapid for the reservoir to react. A lower explosive energy, between 8×10^9 to 2×10^{11} J, could be achieved through volumetric energy released by steam expansion (0.5 to 1.8 MJ/m^3; Table 2). The total eruption energy was independently estimated at 2.1×10^{13} J by Lube et al. (2014) based on an empirical crater-size/energy relationship and on the mass and velocity of ejecta. A value of 3×10^{12} J was estimated by Jolly et al. (2014) based on acoustic data, but this only accounts for the energy coupled to air, and not to the ground, and thus is highly uncertain (Jolly, pers. communication). Of the total energy, $\sim$50% was released by the western blast (Jolly et al., 2014; Lube et al., 2014), which corresponds to about $\sim 1 \times 10^{13}$ J. The uppermost value obtained from the steam flashing condition ($\sim 10^{12}$ J) lies within error of both estimates of Lube et al. (2014) and Jolly et al. (2014).

Our calculation shows that the energy released solely by the process of flashing of liquid water could explain the eruption with no further gas-pressure (e.g., from magmatic gases) supply. Nevertheless, dissolved gases (e.g. CO_2) in the hydrothermal fluids could also have been present, either due to normal magma degassing or related to the precursory fluid injection. These gases would drive the liquid stability field toward lower temperatures and enhance the explosivity compared to pure water (Hurwitz et al., 2016; Thiéry and Mercury, 2008; Thiéry et al., 2010). This ex-
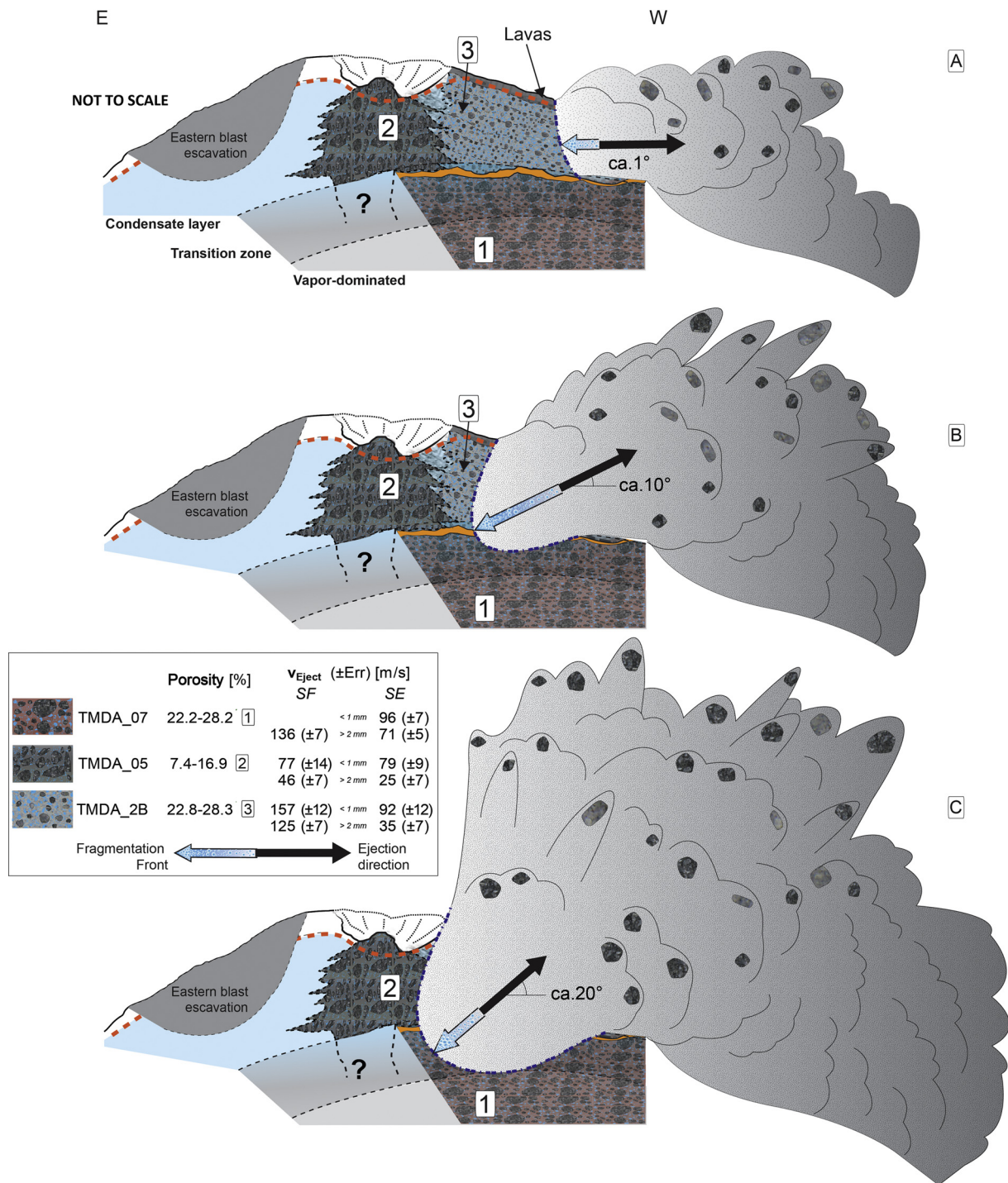
Fig. 7. Conceptual model of the fragmentation and ejection processes of the westward directed blast during the Te Maari eruption. In the legend the ejection velocity are referred to particles smaller than 1 mm and larger than 2 mm (see also Table 2). In this simplified model the lithology is assumed to correspond to the tuff breccia and agglutinated (having a different porosity and lithologic texture) used as sample material for the decompression experiments, being representative for the eruption source area. The length of the "Fragmentation Front" arrow give an idea of the fragmentation speed within the different lithology. Weaknesses represented by 1) a paleo-morphology, 2) sub-horizontal bedding of the variably cemented and agglutinated breccias ponded against the slope of Te Maari Trig to the south, and 3) the debris avalanche failure geometry, led to strong lateral jetting. The model is based on the ballistic lithology and distribution (Breard et al., 2014), and assumes a top–down model (McKibbin et al., 2009) with the downward migration of the explosive process. An initial shallow-seated locus of the explosive boiling fragmented part of lava flows (Breard et al., 2014) and layers of tuff breccia, ejecting ballistic blocks at a very low-launching angle (∼1°; A). Following this, the fragmentation front may have migrated eastward and deeper into more porous breccias and agglutinates (as represented by TMDA_2B and 07). These rock types disintegrated into fine ash, which likely generated surges, while weakly embedded dense enclaves from the matrix of these materials were then easily launched as ballistics. During this phases (B, C) the ejection angle increase (up to 10–20°) as the focal depth of explosion deepened.

tra gas would explain the difference between our and the better-constrained energetic estimation from Lube et al. (2014).

Experimental results also suggest that only steam flashing would be energetic enough to launch fragmented particles at speeds (120–136 m/s) estimated for ballistic from both field data and numerical modeling (Breard et al., 2014; Fitzgerald et al., 2014). Additionally, experiments on TMDA_07 and 2B samples showed how the steam flashing mechanism accelerated abundant fine material out to front velocities of ∼160 m/s. Ejection of this fine material, well coupled with gas expansion, likely drove the surges associated with the Te Maari blast. However, the friction between the erupting material (both fluid and rock) and the conduit walls, may have reduced the kinetic energy available for clast ejection (Mastin, 1995). If the induced boiling front started in the shallow part of the hydrothermal system, and explosions migrated deeper it (Fig. 7), the friction component would have been more important only in the late stages of the eruption. Thus the experimental ejection velocity for fine material is likely a good indicator of initial surge velocity, and it is indeed comparable to estimates (>100 m/s) of Lube et al. (2014) based upon field data. Moreover, the uniform distribution in the highest density ballistic strewn-field (Fig. 7 of Breard et al., 2014), corresponds to an almost elliptical area (1 × 0.5 km large) perpendicular to the axis of the fissure, suggesting that they were only weakly affected by friction against the fissure wall.

According to a top–down eruption model (McKibbin et al., 2009), steam flashing terminates once the rate of groundwater boiling slows and gives way to steam expansion and cessation of ballistic ejection. Additionally, the deepening and eastward opening of the fragmentation front, led to encountering of rocks similar to the TMDA_05 breccias or solid lavas, causing a corresponding drop in explosive energy due to their lower porosity.

4.6. Broader implications

Hydrothermally active areas are common on stratovolcano flanks and old caldera systems. The combined presence of highly pressurized and hot fluids, together with variably altered rocks, makes these areas very sensitive to sudden pressure changes (fluid injections, landslides, etc.), increasing the likelihood of hydrothermal eruptions. In this framework our results lead us to infer that liquid dominated hydrothermal systems, which represent a vast majority (Stimac et al., 2015), may be affected by more energetic eruptions with respect to steam-dominated ones. Based on our estimates the energy released by flashing of liquid water is about one order of magnitude higher than that associated with gas or steam expansion. Furthermore the (connected) porosity of the rocks hosting the hydrothermal system controls the amount of stored energy, with higher porosities resulting in higher energies.

Whether this stored energy is explosively released depends on the lithology of the hydrothermal system host rocks and their petrophysical properties. This also influences their fragmentation process. Rocks characterizing volcanic edifices and vent areas are commonly very heterogeneous. Our results indicate that eruptions involving altered heterogeneous material may generate both large quantities of very fine material (i.e., ash plumes or dilute density currents), together with larger fragments (analogous to ballistics).

Our results further suggest that hydrothermal systems under high temperatures and pressures (∼150 °C–350 °C and 10–100 bar; Stimac et al., 2015), where liquid water is present, will produce highly energetic eruptions. For instance, the destabilization of hydrothermal systems that are >250 °C, and with >20% porosity filled with water in a liquid state, may result in very energetic eruption (>10¹² J), and ballistic blocks ejected with velocities of over 120 m/s.

5. Conclusions

The 6th August 2012 hydrothermal eruption at Upper Te Maari crater was triggered by a landslide on the western flank, unroofing a pressurized hydrothermal system. The experiments reported in this study demonstrate the mechanism driving the eruption was steam flashing, and allow an estimation of the energy budget.

Our rapid decompression experiment setup on natural hydrothermally altered samples (tuff breccias and agglutinates) and the conditions (260 °C–6 MPa and 300 °C–5 MPa) are representative of the shallow condensed layer and the vapor-dominated region envisaged below the Te Maari eruption source area. The triggered decompression mimics the hydrothermal eruption mechanism well, allowing exploration of the effect of different pressure and temperature conditions (determining the fluid state), quantity of stored energy and influences of rock strength and porosity. Our findings include:

1) While the pressure–temperature condition of the hydrothermal system, could be consistent with both water vapor or liquid-to-vapor (flashing) expansion, the latter is significantly more energetic and far more likely to explain eruptions like the Upper Te Maari event;
2) The rock porosity influences the amount of stored energy, with higher porosities accounting for higher energies;
3) Higher porosities also lead to greater production of fine material, because more energy (steam flashing or steam expansion) is available. Furthermore, at a constant porosity, weaker porous tuff breccias and agglutinates produce more fines than the firmly cemented enclave-rich breccia. Additionally the very dense lava enclaves embedded in the matrix of the breccias and agglutinate often remain unfragmented;
4) For higher porosities, particles are jetted ahead of the fragmentation front with higher ejection velocities. In particular, smaller particles (<2 mm) are better coupled with the gas and are ejected more rapidly (>160 m/s) than the larger "ballistic" clasts (>120 m/s) which are rapidly decoupled from the expanding gas;
5) For the investigated Te Maari case the comparison of the field data with the experimental results, together with analytical modeling yields robust estimates for the energy partitioning in this violent hydrothermal eruption. Host rock lithology, appears to control the eruption dynamics and energy partitioning. The strong westward blast generated during the Te Maari eruption, released half of the total energy of the whole eruption, and was sustained by the process of liquid water flashing to steam.

In a broader sense, phase changes during decompression together with the rock type, porosity and rock strength are important fragmentation variables that should be considered for hazard assessment and modeling of eruptions in hydrothermally active environments.

anonymous reviewer and the editor, Tamsin Mather which helped to improve the paper.

References

Alatorre-Ibargüengoitia, M.A., Scheu, B., Dingwell, D.B., Delgado-Granados, H., Taddeucci, J., 2010. Energy consumption by magmatic fragmentation and pyroclast ejection during Vulcanian eruptions. Earth Planet. Sci. Lett. 291, 60–69. http://dx.doi.org/10.1016/j.epsl.2009.12.051.

Alatorre-Ibargüengoitia, M.A., Scheu, B., Dingwell, D.B., 2011. Influence of the fragmentation process on the dynamics of Vulcanian eruptions: an experimental approach. Earth Planet. Sci. Lett. 302, 51–59. http://dx.doi.org/10.1016/j.epsl.2010.11.045.

Alatorre-Ibargüengoitia, M.A., Delgado-Granados, H., Dingwell, D.B., 2012. Hazard map for volcanic ballistic impacts at Popocatépetl volcano (Mexico). Bull. Volcanol. 74, 2155–2169. http://dx.doi.org/10.1007/s00445-012-0657-2.

Alidibirov, M., Dingwell, D.B., 2000. Three fragmentation mechanisms for highly viscous magma under rapid decompression. J. Volcanol. Geotherm. Res. 100, 413–421. http://dx.doi.org/10.1016/S0377-0273(00)00149-9.

Anderson, R.E., 1971. Thin skin distension in Tertiary rocks of southeastern Nevada. Geol. Soc. Am. Bull. 82, 43–58.

Barberi, F., Bertagnini, A., Landi, P., Principe, C., 1992. A review on phreatic eruptions and their precursors. J. Volcanol. Geotherm. Res. 52, 231–246. http://dx.doi.org/10.1016/0377-0273(92)90046-G.

Breard, E.C.P., Lube, G., Cronin, S.J., Fitzgerald, R., Kennedy, B., Scheu, B., Montanaro, C., White, J.D.L., Tost, M., Procter, J.N., Moebis, A., 2014. Using the spatial distribution and lithology of ballistic blocks to interpret eruption sequence and dynamics: August 6 2012 Upper Te Maari eruption, New Zealand. J. Volcanol. Geotherm. Res. 286, 373–386. http://dx.doi.org/10.1016/j.jvolgeores.2014.03.006.

Breard, E.C.P., Lube, G., Cronin, S.J., Valentine, G.A., 2015. Transport and deposition processes of the hydrothermal blast of the 6 August 2012 Te Maari eruption, Mt. Tongariro. Bull. Volcanol. 77, 100. http://dx.doi.org/10.1007/s00445-015-0980-5.

Bromley, C.J., 1999. Tongariro-Tokaanu resistivity structure from magneto-telluric soundings. In: 21st New Zealand Geothermal, Workshop, pp. 119–126.

Browne, P.R.L., Lawless, J.V., 2001. Characteristics of hydrothermal eruptions, with examples from New Zealand and elsewhere. Earth-Sci. Rev. 52, 299–331. http://dx.doi.org/10.1016/S0012-8252(00)00030-1.

Christenson, B.W., Britten, K.W., Mazot, A., Fitzgearld, J., 2013. The 2012 eruption of Te Maari: pre- and post-eruption gas signatures from the magmatic-hydrothermal system. In: Te Maari Day – A Workshop to Discuss Scientific Advances from the 2012 Te Maari Eruption Held at Council Office, Turangi, 22 March 2013, 28 pp.

Fagents, S.A., Wilson, L., 1993. Explosive volcanic eruptions – VII. The ranges of pyroclasts ejected in transient volcanic explosions. Geophys. J. Int. 113, 359–370.

Fitzgerald, R.H., Tsunematsu, K., Kennedy, B.M., Breard, E.C.P., Lube, G., Wilson, T.M., Jolly, A.D., Pawson, J., Rosenberg, M.D., Cronin, S.J., 2014. The application of a calibrated 3D ballistic trajectory model to ballistic hazard assessments at Upper Te Maari, Tongariro. J. Volcanol. Geotherm. Res. 286, 248–262. http://dx.doi.org/10.1016/j.jvolgeores.2014.04.006.

Fowler, A.C., Scheu, B., Lee, W.T., McGuinness, M.J., 2010. A theoretical model of the explosive fragmentation of vesicular magma. Proc. R. Soc. A, Math. Phys. Eng. Sci. 466, 731–752. http://dx.doi.org/10.1098/rspa.2009.0382.

Galland, O., Gisler, G.R., Haug, O.T., 2014. Morphology and dynamics of explosive vents through cohesive rock formations. J. Geophys. Res., Solid Earth 119, 4708–4728. http://dx.doi.org/10.1002/2014JB011050.

Goto, A., Taniguchi, H., Yoshida, M., Ohba, T., Oshima, H., 2001. Effects of explosion energy and depth to the formation of blast wave and crater: field explosion experiment for the understanding of volcanic explosion. Geophys. Res. Lett. 28, 4287–4290. http://dx.doi.org/10.1029/2001GL013213.

Haug, Ø.T., Galland, O., Gisler, G.R., 2013. Experimental modelling of fragmentation applied to volcanic explosions. Earth Planet. Sci. Lett. 384, 188–197. http://dx.doi.org/10.1016/j.epsl.2013.10.004.

Hobden, B.J., 1997. Modelling magmatic trends in time and space: eruptive and magmatic history of Tongariro volcanic complex, New Zealand. PhD Thesis. University of Canterbury, Christchurch.

Hurst, T., Jolly, A.D., Sherburn, S., 2014. Precursory characteristics of the seismicity before the 6 August 2012 eruption of Tongariro volcano, North Island, New Zealand. J. Volcanol. Geotherm. Res. 286, 294–302. http://dx.doi.org/10.1016/j.jvolgeores.2014.03.004.

Hurwitz, S., Clor, L.E., McCleskey, R.B., Nordstrom, D.K., Hunt, A.G., Evans, W.C., 2016. Dissolved gases in hydrothermal (phreatic) and geyser eruptions at Yellowstone National Park, USA. Geology 44, G37478.1. http://dx.doi.org/10.1130/G37478.1.

Jolly, A.D., Jousset, P., Lyons, J.J., Carniel, R., Fournier, N., Fry, B., Miller, C., 2014. Seismo-acoustic evidence for an avalanche driven phreatic eruption through a beheaded hydrothermal system: an example from the 2012 Tongariro eruption. J. Volcanol. Geotherm. Res. 286, 317–330. http://dx.doi.org/10.1016/j.jvolgeores.2014.04.007.

Kato, A., Terakawa, T., Yamanaka, Y., Maeda, Y., Horikawa, S., Matsuhiro, K., Okuda, T., 2015. Preparatory and precursory processes leading up to the 2014 phreatic eruption of Mount Ontake, Japan. Earth Planets Space 67, 111. http://dx.doi.org/10.1186/s40623-015-0288-x.

Kilgour, G., Manville, V., Della Pasqua, F., Graettinger, A., Hodgson, K.A, Jolly, G.E., 2010. The 25 September 2007 eruption of Mount Ruapehu, New Zealand: directed ballistics, surtseyan jets, and ice-slurry lahars. J. Volcanol. Geotherm. Res. 191, 1–14. http://dx.doi.org/10.1016/j.jvolgeores.2009.10.015.

Koyaguchi, T., Scheu, B., Mitani, N.K., Melnik, O., 2008. A fragmentation criterion for highly viscous bubbly magmas estimated from shock tube experiments. J. Volcanol. Geotherm. Res. 178, 58–71. http://dx.doi.org/10.1016/j.jvolgeores.2008.02.008.

Kueppers, U., Scheu, B., Spieler, O., Dingwell, D.B., 2006. Fragmentation efficiency of explosive volcanic eruptions: a study of experimentally generated pyroclasts. J. Volcanol. Geotherm. Res. 153, 125–135. http://dx.doi.org/10.1016/j.jvolgeores.2005.08.006.

Lavallée, Y., Varley, N.R., Alatorre-Ibargüengoitia, M.A., Hess, K.U., Kueppers, U., Mueller, S., Richard, D., Scheu, B., Spieler, O., Dingwell, D.B., 2012. Magmatic architecture of dome-building eruptions at Volcán de Colima, Mexico. Bull. Volcanol. 74, 249–260. http://dx.doi.org/10.1007/s00445-011-0518-4.

Lube, G., Breard, E.C.P., Cronin, S.J., Procter, J.N., Brenna, M., Moebis, A., Pardo, N., Stewart, R.B., Jolly, A., Fournier, N., 2014. Dynamics of surges generated by hydrothermal blasts during the 6 August 2012 Te Maari eruption, Mt. Tongariro, New Zealand. J. Volcanol. Geotherm. Res. 286, 348–366. http://dx.doi.org/10.1016/j.jvolgeores.2014.05.010.

Mastin, L.G., 1991. The roles of magma and groundwater in the phreatic eruptions at Inyo Craters, Long Valley Caldera, California. Bull. Volcanol. 53, 579–596.

Mastin, L.G., 1995. Thermodynamics of gas and steam-blast eruptions. Bull. Volcanol. 57, 85–98. http://dx.doi.org/10.1007/BF00301399.

Mayer, K., Scheu, B., Gilg, H.A., Heap, M.J., Kennedy, B.M., Lavallée, Y., Letham-Brake, M., Dingwell, D.B., 2015. Experimental constraints on phreatic eruption processes at Whakaari (White Island volcano). J. Volcanol. Geotherm. Res. 302, 150–162. http://dx.doi.org/10.1016/j.jvolgeores.2015.06.014.

McGuinness, M.J., Scheu, B., Fowler, A.C., 2012. Explosive fragmentation criteria and velocities for vesicular magma. J. Volcanol. Geotherm. Res. 237–238, 81–96. http://dx.doi.org/10.1016/j.jvolgeores.2012.05.019.

McKibbin, R., Smith, T.A., Fullard, L., 2009. Components and phases: modeling progressive hydrothermal eruptions. ANZIAM J. 50, 365–380. http://dx.doi.org/10.1017/S144618110900011X.

Miller, C.A., Williams-Jones, G., 2016. Internal structure and volcanic hazard potential of Mt Tongariro, New Zealand, from 3D gravity and magnetic models. J. Volcanol. Geotherm. Res. 319, 12–28. http://dx.doi.org/10.1016/j.jvolgeores.2016.03.012.

Montanaro, C., Scheu, B., Gudmundsson, M.T., Vogfjörd, K., Reynolds, H.I., Dürig, T., Strehlow, K., Rott, S., Reuschlé, T., Dingwell, D.B., 2016. Multidisciplinary constraints of hydrothermal explosions based on the 2013 Gengissig lake events, Kverkfjöll volcano, Iceland. Earth Planet. Sci. Lett. 434, 308–319. http://dx.doi.org/10.1016/j.epsl.2015.11.043.

Mueller, S., Scheu, B., Kueppers, U., Spieler, O., Richard, D., Dingwell, D.B., 2011. The porosity of pyroclasts as an indicator of volcanic explosivity. J. Volcanol. Geotherm. Res. 203, 168–174. http://dx.doi.org/10.1016/j.jvolgeores.2011.04.006.

Muffler, L.J.P., White, D.E., Truesdell, A.H., 1971. Hydrothermal explosion craters in Yellowstone National Park. Bull. Geol. Soc. Am. 82, 723–740. http://dx.doi.org/10.1130/0016-7606(1971)82[723:HECIYN]2.0.CO;2.

Pardo, N., Cronin, S.J., Németh, K., Brenna, M., Schipper, C.I., Breard, E., White, J.D.L., Procter, J., Stewart, B., Agustín-Flores, J., Moebis, A., Zernack, A., Kereszturi, G., Lube, G., Auer, A., Neall, V., Wallace, C., 2014. Perils in distinguishing phreatic from phreatomagmatic ash; insights into the eruption mechanisms of the 6 August 2012 Mt. Tongariro eruption, New Zealand Natalia. J. Volcanol. Geotherm. Res. 286, 397–414.

Planas-Cuchi, E., Salla, J.M., Casal, J., 2004. Calculating overpressure from BLEVE explosions. J. Loss Prev. Process Ind. 17, 431–436. http://dx.doi.org/10.1016/j.jlp.2004.08.002.

Procter, J.N., Cronin, S.J., Zernack, A.V., Lube, G., Stewart, R.B., Nemeth, K., Keys, H., 2014. Debris flow evolution and the activation of an explosive hydrothermal system, Te Maari, Tongariro, New Zealand. J. Volcanol. Geotherm. Res. 286, 303–316. http://dx.doi.org/10.1016/j.jvolgeores.2014.07.006.

Prugh, R.W., 1991. Quantitative evaluation of "Bleve" Hazards. J. Fire Prot. Eng. 3, 9–24. http://dx.doi.org/10.1177/104239159100300102.

Rager, A.H., Smith, E.I., Scheu, B., Dingwell, D.B., 2014. The effects of water vaporization on rock fragmentation during rapid decompression: implications for the formation of fluidized ejecta on Mars. Earth Planet. Sci. Lett. 385, 68–78. http://dx.doi.org/10.1016/j.epsl.2013.10.029.

Scheu, B., Spieler, O., Dingwell, D.B., 2006. Dynamics of explosive volcanism at Unzen volcano: an experimental contribution. Bull. Volcanol. 69, 175–187. http://dx.doi.org/10.1007/s00445-006-0066-5.

Scheu, B., Kueppers, U., Mueller, S., Spieler, O., Dingwell, D.B., 2008. Experimental volcanology on eruptive products of Unzen volcano. J. Volcanol. Geotherm. Res. 175, 110–119. http://dx.doi.org/10.1016/j.jvolgeores.2008.03.023.

Sparks, R.S.J., Bursik, M.I., Carey, S.N., Gilbert, J.S., Glaze, L.S., Sigurdsson, H., Woods, A.W., 1997. Volcanic Plumes. John Wiley and Sons, Chichester, United Kingdom.

Spieler, O., Kennedy, B., Kueppers, U., Dingwell, D.B., Scheu, B., Taddeucci, J., 2004. The fragmentation threshold of pyroclastic rocks. Earth Planet. Sci. Lett. 226, 139–148. http://dx.doi.org/10.1016/j.epsl.2004.07.016.

Stimac, J., Goff, F., Goff, C.J., 2015. Intrusion-related geothermal systems A2. In: Sigurdsson, Haraldur, et al. (Eds.), The Encyclopedia of Volcanoes, second edition. Academic Press, Amsterdam, pp. 799–822, Chapter 46.

Taddeucci, J., Valentine, G.A., Sonder, I., White, J.D.L., Ross, P.S., Scarlato, P., 2013. The effect of pre-existing craters on the initial development of explosive volcanic eruptions: an experimental investigation. Geophys. Res. Lett. 40, 507–510. http://dx.doi.org/10.1002/grl.50176.

Thiéry, R., Mercury, L., 2008. Explosive properties of water in volcanic and hydrothermal systems. In: ICPWS XV, p. 7.

Thiéry, R., Mercury, L., 2009. Explosive properties of water in volcanic and hydrothermal systems. J. Geophys. Res., Solid Earth 114, 1–19. http://dx.doi.org/10.1029/2008JB005742.

Thiéry, R., Loock, S., Mercury, L., 2010. Explosive properties of superheated aqueous solutions in volcanic and hydrothermal systems. In: Metastable Systems under Pressure, pp. 293–310.

Valentine, G.A., Graettinger, A.H., Macorps, É., Ross, P.-S., White, J.D.L., Döhring, E., Sonder, I., 2015. Experiments with vertically and laterally migrating subsurface explosions with applications to the geology of phreatomagmatic and hydrothermal explosion craters and diatremes. Bull. Volcanol. 77. http://dx.doi.org/10.1007/s00445-015-0901-7.

Walsh, F.D., Hochstein, M.P., Bromley, C.J., 1998. The Tongariro geothermal system (NZ): review of geophysical data. In: Proc. 20th NZ Geotherm. Work, pp. 317–324.

Yamamoto, T., 2014. The pyroclastic density currents generated by the September 27, 2014 phreatic eruption of Ontake Volcano, Japan. Bull. Geol. Surv. Jpn. 65 (9), 117–127.

Yokoo, A., Goto, A., Taniguchi, H., Oshima, H., 2002. Energy and depth of Usu 2000 phreatic explosions. Geophys. Res. Lett. 29, 48–51. http://dx.doi.org/10.1029/2002GL015928.